RESEARCH ARTICLE

Deep Impact: Excavating Comet Tempel 1

M. F. A'Hearn,[1]* M. J. S. Belton,[2] W. A. Delamere,[3] J. Kissel,[4] K. P. Klaasen,[5] L. A. McFadden,[1] K. J. Meech,[6] H. J. Melosh,[7] P. H. Schultz,[8] J. M. Sunshine,[9] P. C. Thomas,[10] J. Veverka,[10] D. K. Yeomans,[5] M. W. Baca,[9] I. Busko,[11] C. J. Crockett,[1] S. M. Collins,[5] M. Desnoyer,[10] C. A. Eberhardy,[8] C. M. Ernst,[8] T. L. Farnham,[1] L. Feaga,[1] O. Groussin,[1] D. Hampton,[12] S. I. Ipatov,[1] J.-Y. Li,[1] D. Lindler,[13] C. M. Lisse,[1,14] N. Mastrodemos,[5] W. M. Owen Jr.,[5] J. E. Richardson,[7,10] D. D. Wellnitz,[1] R. L. White[11]

Deep Impact collided with comet Tempel 1, excavating a crater controlled by gravity. The comet's outer layer is composed of 1- to 100-micrometer fine particles with negligible strength (<65 pascals). Local gravitational field and average nucleus density (600 kilograms per cubic meter) are estimated from ejecta fallback. Initial ejecta were hot (>1000 kelvins). A large increase in organic material occurred during and after the event, with smaller changes in carbon dioxide relative to water. On approach, the spacecraft observed frequent natural outbursts, a mean radius of 3.0 ± 0.1 kilometers, smooth and rough terrain, scarps, and impact craters. A thermal map indicates a surface in equilibrium with sunlight.

Our knowledge of the interior structure of comets, particularly of the evolution of the outer layers at successive perihelion passages, is almost unconstrained by data and relies instead primarily on theoretical models. Thus, the relation of the coma's composition to the solid composition of the nucleus is uncertain. The Deep Impact (DI) mission, in which a spacecraft would collide with and excavate a cometary nucleus, was conceived, proposed to, and selected by NASA to address this very point (*1*). DI delivered an impact of 19 GJ of kinetic energy to the nucleus of comet 9P/Tempel 1 on 4 July 2005 at about 05:44:36 UT (Earth-received time 05:52:02 UT).

The primary goals of the mission were to determine the differences between the surface of a comet with its ambient outgassing and its interior, which might contain enhanced volatiles, and to determine the structural properties and strength of the surface layers.

DI consisted of two fully functional spacecraft: an impacting spacecraft weighing 364 kg (plus 6.5 kg of unused hydrazine fuel, N_2H_4, at time of impact) and a flyby spacecraft for observing the impact and relaying data from the impactor. The impactor used an autonavigation system to analyze images of the comet and target the impactor at a site on the nucleus that would be in sunlight and visible from the flyby spacecraft. Impact speed was 10.3 km/s. The impactor was 49% copper to minimize chemical reactions with water in the comet that would lead to bright emission features. The two spacecraft separated 24 hours before impact, at which point the flyby spacecraft diverted to miss the nucleus by 500 km and slowed down by 100 m/s to provide an 800-s viewing window after impact. At 500 km before closest approach, the flyby spacecraft froze in an attitude that kept its dust shields in the proper orientation. After passing through the innermost coma, the spacecraft turned and looked back at the comet to take additional data (*2*, *3*). The event was also recorded at nearly all the world's remote observing facilities, both ground-based and space-based, to provide more extensive coverage in both time and space than was possible from a flyby mission (*4*).

The Comet Before Impact

The nucleus. The comet was observed by the flyby spacecraft almost continuously from several days before impact until impact and at 4-hour intervals for weeks before the nearly continuous observing. In addition, the impactor obtained images beginning shortly after release from the flyby until ~4 s before impact. The only comet that has been comparably well studied is comet Halley at its 1986 apparition. Figure 1 shows a composite of several images from the impactor, with the highest resolution in the vicinity of the impact site.

The shape of the nucleus is incompletely determined because the slow rotation period, 40.7 hours, and the high velocity of the flyby resulted in only slightly more than half the surface being illuminated and resolved. However, the nucleus was in full silhouette after the flyby, backlit by ejecta from the impact, which strongly constrains the mean radius. Images from the medium resolution instrument (MRI) covered ~25% of the object with sufficient stereo convergence and resolution to solve for 70 control points in 43 images, with an average relative uncertainty of <30 m. The positive spin pole was determined to be within 10° of RA = 5°, Dec = 78°. This solution compares favorably with a pre-encounter measurement of RA = 46°, Dec = 73° based on light curve analysis (*5*). The spin vector was constrained by the projected spin axis found in approach images, combined with matching outlines of the body in images before and after the encounter.

The control points, in combination with limb outlines, restrict the shape for slightly more than half the area, but some longitudes remain unobserved. The mean radius of the model is estimated to have been 3.0 ± 0.1 km in

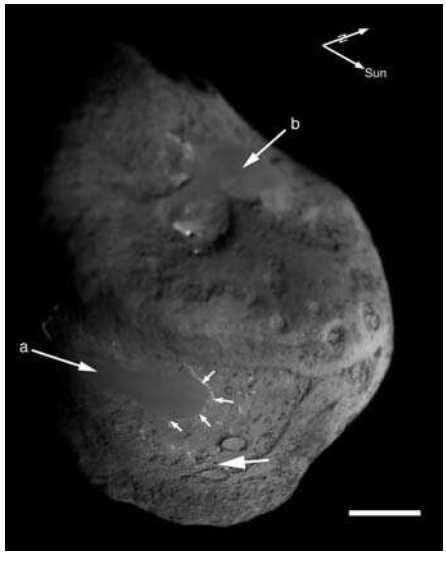

Fig. 1. Composite of ITS images. The Sun is to the right and celestial north is toward the upper right, near the rotational pole. Ecliptic north is another 20° counterclockwise from the north pole. Arrows a and b point to the large, smooth areas. The impact site is indicated by the other large arrow. The small arrows highlight the scarp, bright due to the illumination angle, which shows the smooth area to be elevated above the extremely rough terrain. The scale bar is 1 km, and the two arrows above the nucleus point to the Sun and to the rotational axis of the nucleus. Celestial north is near the rotational pole; ecliptic north is more nearly upward.

[1]University of Maryland, College Park, MD 20742, USA. [2]Belton Space Exploration Initiatives, Tucson, AZ 85716, USA. [3]Delamere Support Services, Boulder, CO 80301, USA. [4]Max-Planck-Institute for Solar System Research, Katlenburg-Lindau, D37191 Germany. [5]Jet Propulsion Laboratory, Pasadena, CA 91109, USA. [6]University of Hawaii, Honolulu, HI 96822, USA. [7]University of Arizona, Tucson, AZ 85721, USA. [8]Brown University, Providence, RI 02412, USA. [9]SAIC, Chantilly, VA 20151, USA. [10]Cornell University, Ithaca, NY 14853, USA. [11]Space Telescope Science Institute, Baltimore, MD 21218, USA. [12]Ball Aerospace and Technology Corporation, Boulder, CO 80301, USA. [13]Sigma Scientific, Greenbelt, MD 20771, USA. [14]Applied Physics Laboratory, Johns Hopkins University, Laurel, MD 20723, USA.

*To whom correspondence should be addressed. E-mail: ma@astro.umd.edu

good agreement with pre-encounter estimates (*5*, *6*); the longest dimension is 7.6 km and the shortest is 4.9 km, which implies much less elongation than pre-encounter estimates (*5*, *6*).

The shape model indicates that the incidence angle of the impactor was 34° from the local horizontal, slightly higher than estimated from the foreshortening of the large features near the impact site if one assumes that they are circular. However, our present shape model is not as well constrained at the impact site by control points as is the rest of the visible area, because it was obscured by the ejecta after impact.

DI high-resolution images cover about 30% of the nucleus at <10 m/pixel. A region about 2 km across, including the impact site, was imaged at slightly better resolution by the impactor targeting sensor (ITS) shortly before impact.

The observed part of the nucleus contains several regions of distinct morphology, which suggests considerable variation of exposed materials, geologic processes, and ages. Two different areas, basically the top and bottom halves of Fig. 1, display several dozen apparently circular features, ranging from 40 to 400 m. The cumulative size-frequency distribution of these features is consistent with impact crater populations. Those features in the bottom part of Fig. 1, near the impact site, appear to be expressed both topographically as circular ridges and as slightly darker material. Those in the top half of the vicinity of the impact site are expressed as depressions, with smooth, unraised rims. The size distribution of these features is different from that of circular depressions on comet Wild 2, the target of the Stardust mission (*7*). The morphology of the Tempel 1 round forms is also distinct from those on Wild 2.

The very bottom of the comet in Fig. 1 appears rough at high emission angles, and it may contain some circular features, but this area cannot be easily interpreted.

Two regions of smooth surface exist (arrows a and b in Fig. 1). One smooth region (arrow a) is bounded to the north by a scarp ~20 m in height. In combination with the appearance of the area to the north, which shows circular features, and the distinctly rougher terrain east and west of the smooth area, the scarp strongly suggests removal by backwasting of a 20-m layer, leaving an exhumed surface containing the circular features. The other smooth area (b) embays two areas of arcuate scarps, possibly bounding degraded circular forms. Both smooth areas are in gravitational lows and area a, at least, is approximately level. The smoothness is reminiscent of the plateau seen on comet Borrelly (*8*), but the surroundings are different.

The smooth surfaces and bounding scarp imply that the nucleus is layered. Banding of albedo, running nearly horizontally in Fig. 1 and at a high angle to the smooth surfaces, suggests either stripping of other layers or exposure of different kinds of layers within the comet.

Overall, the surface of Tempel 1 is remarkably homogeneous in albedo and color. Albedo variations are within 50% of an average of 0.04 (visible wavelength). The brightest small areas are no more than twice as bright as the bulk of the surface. Color ratios between 300 and 1000 nm are uniform to <±2%. No exposures of clean ice or frost have been identified on the basis of albedo or color. It is estimated that Tempel 1 loses some 10^9 kg of material per perihelion passage (*9*). Such a mass, if lost from 10% of the 100 km^2 area of the comet, would lower the surface (density = 1000 kg m^{-3}) by 10 cm per perihelion passage. Alternatively, all of the mass could be supplied by retreat by 50 m of a 1-km-long, 20-m-high scarp. Because there are probably at least several kilometers of such scarps, the observed mass loss could plausibly come from a few meters of retreat of scarps per perihelion passage.

With the infrared (1.05 to 4.8 μm) spectrometer of DI, we obtained three spatial scans of the nucleus that allowed us to map its temperature. We obtained (i) a scan of ~90% of the part of the nucleus visible from DI, ~19 min before impact, with a resolution of ~200 m/pixel, (ii) a scan of 100% of the part of the nucleus visible from DI, ~12 min before impact, with a resolution of ~160 m/pixel, and (iii) a scan of ~50% of the part of the nucleus visible from DI, ~6 min before impact, with a resolution of ~120 m/pixel.

For each scan, we derived the temperature by fitting the data with a model that includes two components: the scattered light from the Sun and a thermal component. For the scattered light, we used a solar spectrum (*10*) reddened by 4% per μm to match the data and normalized between 1.8 μm and 2.2 μm, where we have a good signal-to-noise ratio. The thermal component is a Planck function times the infrared emissivity of the nucleus, which we set to 0.95.

The derived temperature (Fig. 2) varies from 260 ± 6 K to 329 ± 8 K on the sunlit side. The uncertainty is due to an absolute calibration uncertainty of ~20%. The three scans are consistent with each other. The temperature map matches the topography of the nucleus: Shadows are the coolest areas, whereas the hottest areas are close to the subsolar point. This is a good indication that the thermal inertia is low. The maximum temperature of 326 ± 6 K is in excellent agreement with the subsolar point temperature of 325 K for a standard thermal model with no beaming factor (*11*). This agreement is another argument for a low thermal inertia, most probably lower than 100 MKS (MKS = W/K/m^2/$s^{1/2}$), in agreement with our own pre-encounter estimate for Tempel 1 (*12*) and with the inferred low (<15 MKS) thermal inertia on small bodies like Chiron and Chariklo, Asbolus, or main-belt asteroids (*13*–*15*). With our resolution, we do not see areas on the sunlit surface colder than 260 K, well above the temperature expected for sublimation of volatiles on the surface, such as H_2O, CO_2, and/or CO. Therefore, volatiles probably sublime below the surface.

Activity. Precise knowledge of the spin state of the nucleus is the key to linking remotely observed coma phenomena to specific locations on the nucleus. We derived information about the spin of the nucleus from two sources: the fully resolved images and time-series photometry of the unresolved nucleus on approach. The fully resolved

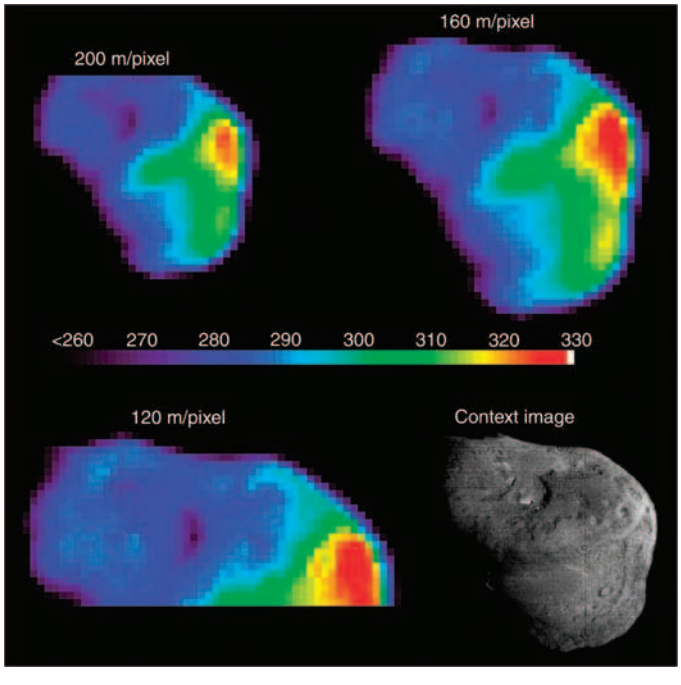

Fig. 2. Temperature maps of the nucleus with different resolutions. The context image is a deconvolved HRI image taken just before impact. The color bar in the middle gives temperatures in kelvins. The last spatial scan, in lower left, was interrupted to begin the sequence of impact observations. The Sun is to the right in all images.

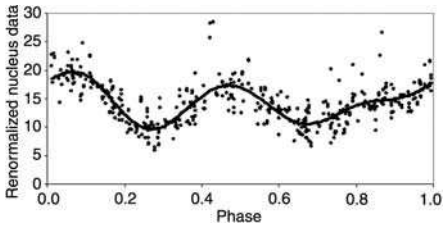

Fig. 3. Renormalized photometric model of the spinning nucleus, based on a four-harmonic least-squares fit to the MRI approach photometry. Zero phase is at the time of impact, JD 2453555.73932. Approach data are phased to $P = 1.701$ days. Most of the scatter comes from variations in the coma signal whose trend has been removed.

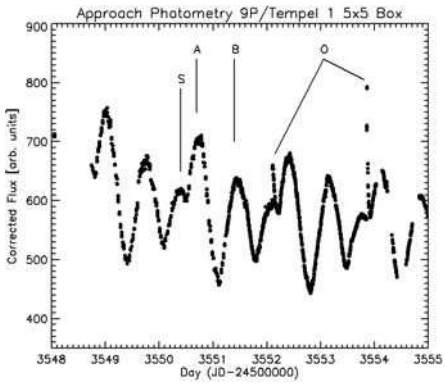

Fig. 4. Normalized rotational light curve immediately preceding encounter. S indicates the shoulder on the increase to peak A. Peak B is much smaller and has no shoulder. O indicates the last two outbursts before impact (at 3555.74 on this scale). Earlier outbursts occur either at this same rotational phase or at the two peaks.

images, using control point geodesy, provide the best estimate of the direction of the spin axis and sense of spin, whereas harmonic analysis of the approach photometry gives the best determination of the spin period.

Photometric coverage of the unresolved cometary nucleus in various color filters began 63.4 days before impact [(I), taken as JD2453555.73932], with samples taken, when possible, about every 4 hours using both the MRI and the high resolution instrument (HRI). At I – 19 days (phase angle 51.3°), a new sequence of images, more densely sampled, was begun for navigational purposes and continued through I – 0.6 days. These two independent databases provide excellent coverage for studies of coma activity, the spin state, and the dependence of nuclear brightness on solar phase angle. An extensive analysis was carried out using MRI data taken through the clear filters and based on 5 by 5 and 15 by 15 pixel arrays centered on the nucleus (*3*).

The resultant rotational variation of the nucleus is shown in Fig. 3, where the fitted curve has a period of 1.701 ± 0.014 days (40.832 ± 0.33 hours) and four harmonics. This should be compared with the pre-encounter prediction of 1.744 ± 0.006 days based on Earth-based observations (*5*). The difference corresponds to a half-cycle or whole-cycle shift between different observing runs.

Observations of the comet before impact detected numerous brief outbursts from the comet. The ambient outgassing results in a coma that is fainter, relative to the nucleus, than the coma of Wild 2 (*1*, *6*, *7*, *16*, *17*), making study of the ambient coma harder but the study of small outbursts easier. Many, but not all, of the outbursts appear to be from one part of the surface (Table 1). Outbursts like these are probably common occurrences for most comets near the Sun. Two obvious outbursts occurred in the week immediately before impact (Fig. 4). Analysis of the rotational phase of the outbursts shows that certainly three and probably four of the outbursts occurred near the start of the "shoulder" feature on the rotational light curve (Fig. 4 and Table 1). This corresponds very roughly to the time of sunrise on the upper surface in Fig. 1, and images taken at the time of the outburst show the ejecta primarily in the northeast quadrant from the nucleus, as expected from the orientation of that face at sunrise. Two outbursts, however, occurred near the two peaks of the light curve, one near each. We therefore see two active areas, one on the well-studied side of the nucleus and the other likely on the unstudied side.

Table 1. Outbursts detected by Deep Impact. Onset occurs at the given Julian day and the corresponding UT date. The height is in arbitrary units and is useful only for estimating a rough amplitude relative to each other and relative to rotational variations of about 250 units from peak A to the subsequent trough (*28*).

Julian day	UT	Height	Rotational phase
2453506.053	May 15 13:16		shoulder?
2453524.888	Jun 3 09:19	300	shoulder
2453536.055	Jun 14 13:19	<100	Peak B
2453543.884	Jun 22 09:13	75	Peak A
2453552.105	Jun 30 14:31	80	shoulder
2453553.857	Jul 2 08:34	240	shoulder

All of the well-observed outbursts are characterized by a very sharp rise (<10 min for the best sampled outburst) (Fig. 5) followed by a slow increase and gradual decay (or dissipation) over roughly an hour, although some signs of the large outbursts can be seen for a considerable portion of a day. We interpret the outburst as being nearly instantaneous (a few minutes or less), followed by some increase in brightness due to decreasing optical depth, with the particles that are dragged out evaporating and/or dispersing into the ambient coma outside the box over which we integrate the brightness on a time scale of a few hours. There is sometimes a residual brightness, no more than about 10% of the peak brightness, which can persist for up to 18 hours. Whether the particles also evaporate is still an open question.

The Cratering Experiment: Morphological Analysis

Impact site and crater. The impactor struck the nucleus near its southern (ecliptic) limb as seen on approach, leading to an oblique impact and the resultant phenomenology. The impact site was determined by analyzing a combination of all images from the impactor and its attitude telemetry (see Fig. 1 and, at higher resolutions, Fig. 6). At about 20 s before impact, a large dust particle hit the impactor, causing the pointing to rapidly slew away. The attitude-control system brought the pointing back more slowly, centering on the impact site again at ~10 s before impact, when another dust particle deflected it again. The last image pointed at the impact site had a scale of 1.2 m/pixel, but the image appears to have a resolution no better than 3 m, which indicates that sandblasting by dust may have degraded the optical quality of the ITS (change of scale during the 100-msec exposure is only about 1% of the actual scale; the degradation does not fit well with smear because of motion). The last image transmitted to Earth was taken about 4 s before impact, but at this time the camera was pointed more than a field of view away from the impact site.

The time of impact was not directly measured but can be inferred. The earliest possible time of impact is constrained by an analysis of the increase of scale in the ITS images and is roughly 05:44:35.4 UTC. The latest possible time of impact is constrained by the appearance of the flash in the high-speed imaging sequence with MRI (Fig. 7), which requires that impact occurred before about 05:44:36.2. Both times are as seen at the spacecraft. Allowing for the light travel time to Earth of 7:26.1, the window

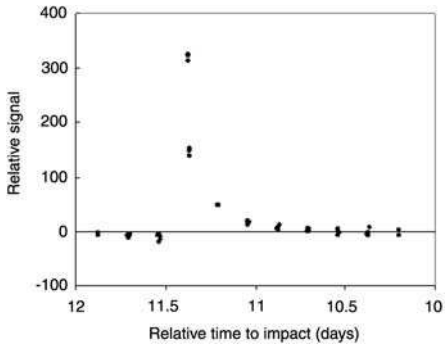

Fig. 5. Brightness profile of outbursts. Data on the two strongest outbursts are combined by applying scaling factors and time shifts. The abrupt rise occurs within 18 min. The brightness falls rapidly at first, followed by a more gradual falloff that clears in ~18 hours.

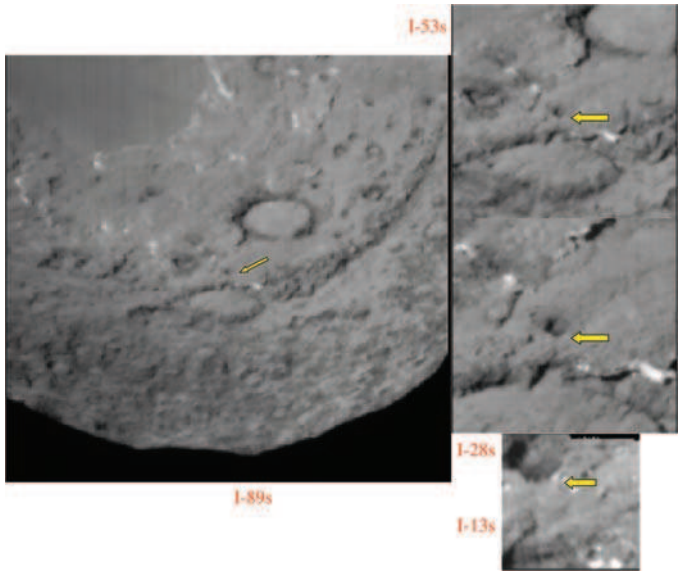

Fig. 6. Impact site at successively higher resolutions. The images were all taken by the impactor at the indicated times before impact. The impact site is indicated by the yellow arrow in each frame.

for the impact time as observed at Earth is 05:52:01.5 to 05:52:02.3.

The final crater has not yet been directly measured because of a large amount of fine dust in the ejecta obscuring our view.

Flash, plume, and early ejecta. The impact was oblique, 20° to 35° from horizontal, and the effects of obliquity appear in several ways. The initial flash (Fig. 7, panels 4 and 5) lasted <200 ms and may have been visible at the entry hole, or it may have been transmitted through the undisturbed layer under which the impactor tunneled. It is probably associated with vaporization of the impactor and part of the comet. The second flash (Fig. 7, panels 6 to 8, and Fig. 8, panel 2) was displaced downrange and saturated the detectors of both cameras for one HRI frame and two MRI frames covering 120 ms leading to the horizontal "bleeding" of charge (Fig. 7, panels 7 and 8, and Fig. 8, panel 2). This may be associated with the first eruption of material at the surface. A plume of hot material (see subsequent discussion of spectra) moved outward (Fig. 7, panels 7 to 10) at a projected velocity of 5 km/s. Depending on the angle with respect to the surface, the true velocity is likely to have been 7 to 10 km/s. This is consistent with laboratory experiments (*18*), which show downrange plumes moving at a speed comparable to that of the impactor. The plume expanded at ~3 km/s, consistent with gas-driven expansion in those laboratory experiments. The temperatures deduced below from spectroscopy suggest that this plume was self-luminous.

The mechanically excavated cone (Fig. 7, panels 9 to 12, and Fig. 8, panels 3 to 8) arises as the second flash drops below saturation, is displaced farther downrange, and consists of much more slowly moving material. Even as the ejecta expand rapidly above the surface, they remain optically thick, as is clear from the shadow cast on the nucleus by the ejecta. The shadow is highlighted by the red arrows in panels 3 and 7 of Fig. 8 (also visible in panels 4 to 6), showing that even many seconds after the start the ejecta are still optically thick. The optical depth producing the initial shadow is $\gg 1$. This is likely because the ejecta are primarily in the form of very small grains, which maximize the cross section per unit mass. The shadow is >300 m across at its base, which is much wider than the expected size of the crater at this early stage; this is undoubtedly due to a spread in the angle of ejection as seen in laboratory experiments.

The peak radiance from the ejecta occurred 3 to 4 s after the impact, and the brightness peak moves downrange at roughly 100 m/s, reflecting the excess of ejecta in the downrange direction. Several rays become obvious (Fig. 8, panels 4 to 8), and they persist until long after the encounter and are initiated at the very beginning of the excavation phase. There are no prominent rays toward the top of the figures. This reflects both the perspective from the spacecraft and an uprange zone of avoidance, with relatively little ejecta, indicated by the yellow arrow in panel 8 of Fig. 8, which is characteristic of oblique impacts (*19*). There is also a highly foreshortened uprange plume visible in Fig. 7 in the first second, similar to plumes seen in laboratory experiments with hypervelocity impact into porous material (*20*). In the experiments, this usually reflects flow back up the entry path. As late as 13 min after impact, the optical depth in ejecta near the limb of the nucleus has dropped only to the range of 2 to 3.

Later ejecta and fallback. The ejecta cone remained attached to the surface throughout the encounter and even through the look-back imaging (Fig. 9). The observation that the ejecta cone remained attached to the surface indicates that formation of the crater was controlled by gravity rather than by strength (*20*, *21*). The volume of ejecta then argues against deep burial of the impactor or compression control of the crater formation (*22*). The geometry in the look-back images is such that the curtain or cone can be no higher than 500 ± 250 m above the surface. With worst-case assumptions for all parameters (height of 750 m at 1 hour after impact, sandlike surface density of 1500 kg m^{-3}), we find an upper limit of 65 Pa (an extremely weak, powderlike substance) for the shear strength of the moderately shocked region around the rim of the final crater.

These look-back images also allowed us to observe the lateral expansion of the conical ejecta curtain for nearly half an hour, as the individual particles that make up the curtain follow ballistic paths in Tempel 1's gravitational field. The curtain itself marks the locus of the solid ejecta in flight at any given time: Its bottom region is composed of particles near the end of their flight and about to land on the surface; its middle region is composed of particles reaching their maximum height above the surface and traveling radially from the center of the cone (and thus parallel to the surface); and the upper portions are composed of particles that have not yet reached their apex, and the uppermost ones are on escape trajectories (*23*). If we assume (i) that the middle and late stages of excavation are not affected by the obliquity of the impact (the cone has become more nearly axially symmetric) as observed in experiments, (ii) that the laboratory-derived scaling relation-

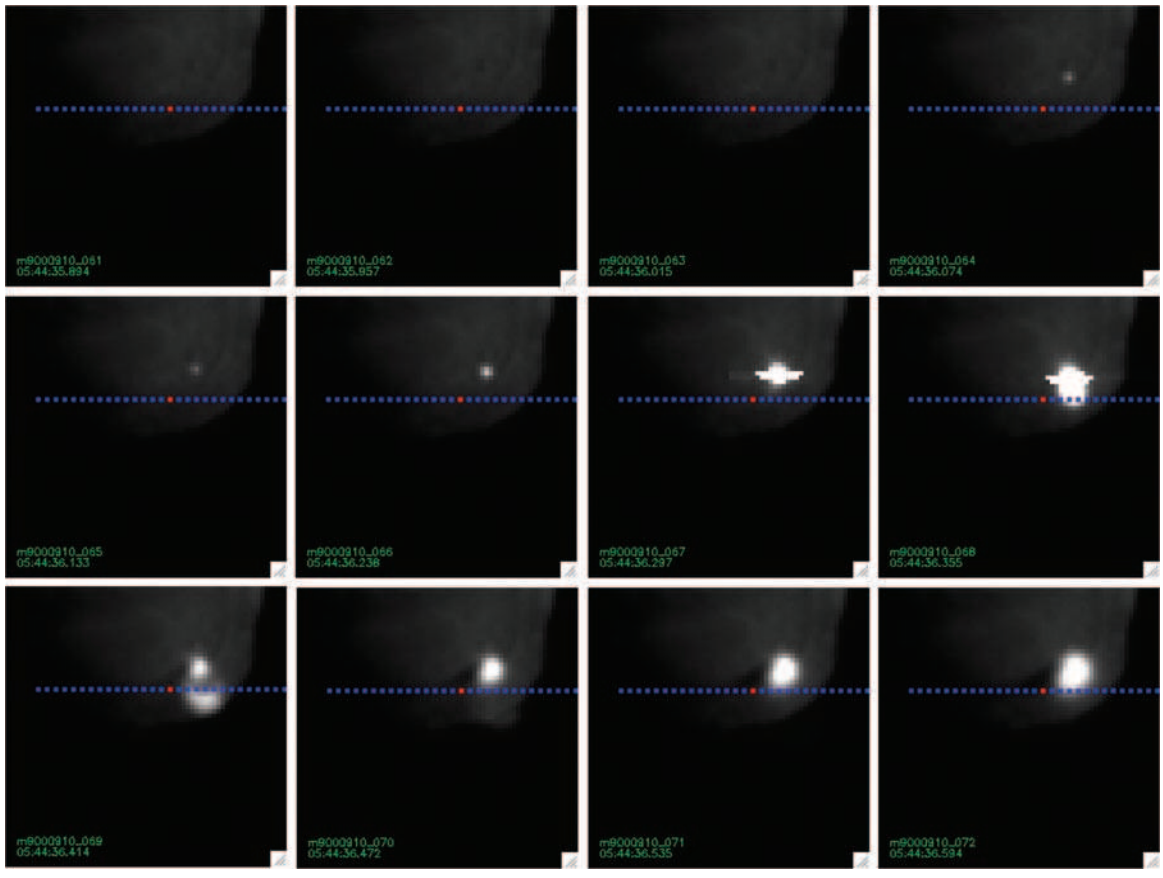

Fig. 7. Images of impact taken with MRI. The blue dotted line is the position of the spectrograph slit. The red point on the blue dotted line is the position along the slit for the spectrum shown in Fig. 11. Panels 1 (top left) through 12 (bottom right) are labeled with time of end of 50-ms exposure, and all images were taken during the exposure of the spectrum.

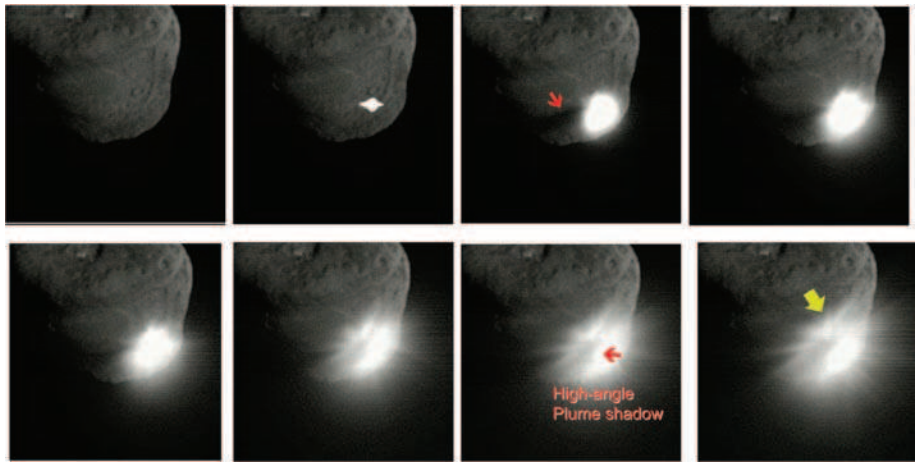

Fig. 8. HRI sequence showing the development of the ejecta. Red arrows highlight shadows due to opacity of the ejecta, whereas the yellow arrow indicates the zone of avoidance in the uprange direction. HRI frames 9000910_005 through 9000910_012 are 100-ms exposures spaced by 0.84 s, ending at 05:44:35.47 through 05:44:41.32.

Fig. 9. Look-back image of comet taken 45 min after impact. The ejecta plume is still connected to the nucleus (the impact site is close to the limb on the far side). The image has been stretched to show the rays at large distances, and this causes the limb of the nucleus and the innermost ejecta cone to saturate.

ships for gravity-dominated cratering (*24*) are valid for our experiment, and (iii) that ejecta flow properties (*25*) extrapolate reasonably well to this particular impact, then the expansion of the base of the conical ejecta can be used to estimate the strength of gravity, as shown in Fig. 10.

Although the shape of the nucleus is far from spherical, this calculation gives a good first approximation to the local gravity at the impact site, 50 + 34/–25 mgal. We then use the preliminary shape model described above to find the uniform density, and thus mass, required to produce the local gravity field, deriving a total mass for the nucleus of 7.2×10^{13} ($+4.8/-3.8 \times 10^{13}$) kg and a bulk density of 620 + 470/–330 kg m^{-3}. In principle, the scaling laws can also be used to predict the size of the crater, but the result depends on assuming a value for the density of the surface layers, which may be different from the bulk density.

The Cratering Experiment: Spectral Analysis

A small subset of the spectra has been carefully calibrated. At the time of impact, the slit was positioned downrange of the impact site (Fig. 7), and spatially resolved spectra were taken as rapidly as possible while material flowed past the slit. The position sampled for the spectrum in Fig. 11 (red dot in Fig. 7) is roughly 85 m

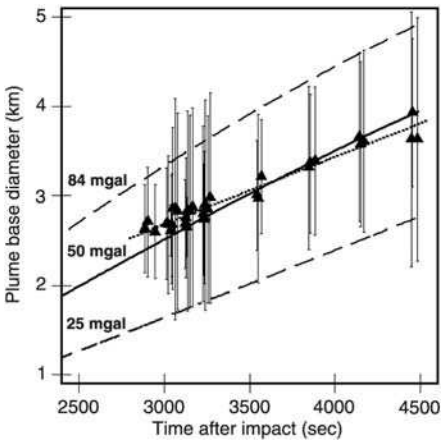

Fig. 10. Expansion of ejecta cone. Measurements of the width of the base of the ejecta cone in look-back images, with a correction of 250 m for the inability to see the actual base of the cone. The curves are numerical calculations (*20*) for various gravitational fields on a spherical nucleus.

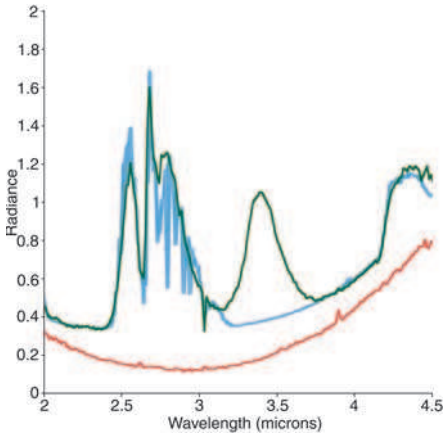

Fig. 11. Spectrum of vapor plume (green) at ~1 + 0.6 s. The blue line is the model described in the text. The model does not include species that contribute to the organic feature at 3.4 μm. The red line is the nuclear spectrum taken 0.7 s earlier.

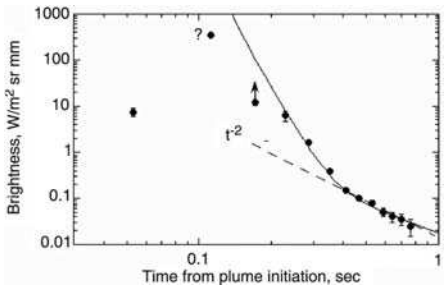

Fig. 12. Brightness of the peak pixel in the plume versus time in MRI frames mv9000910066-78. The point marked ? is a guess at the value for the saturated pixel. The dashed curve is what is expected for uniformly expanding particles reflecting sunlight. The solid curve is the model described in the text. The origin of time is based on extrapolating the motion of the plume back to its origin at constant velocity.

on a side at the comet, centered 0.46 km downrange from the impact site and 0.34 km to the side of the downrange direction. The side of the fast, hot vapor plume was present in the slit only for the last 200 msec of the exposure. The excavated ejecta from the event may be in the field of view for the last 50 msec. The immediately previous spectrum at this pixel, shown in red in Fig. 7, can be adequately described by a combination of reflected light, slightly reddened, and thermal emission at 285 K from the nucleus alone. Any foreground coma is minor compared with the dust and gas in subsequent spectra.

Emission features in the spectrum include those of H_2O, HCN, CO_2, and what is normally called the "organic feature," which corresponds to the C-H stretching-mode vibration in several commonly seen molecules, including H_2CO (formaldehyde) and CH_3OH (methanol). Our spectral resolution is, in general, not sufficient to separate the individual species in the organic feature. Superimposed on the observed spectrum is a model spectrum that includes the observed nuclear spectrum shown in red, hot (850 K) dust, and the three identified species. Organics are not included in the model. The model assumes a rotational excitation temperature of 1400 K, but both the H_2O and the CO_2 can be adequately fit with a wide range of temperatures, roughly 1000 K to 2000 K. A calculation of fluorescent emission shows that the emissions are optically thick, requiring an extensive model to separate temperature broadening from optical depth and to determine relative abundances.

In the succeeding spectrum, for which the plume was not present and only ejecta were moving across the slit, the reflected continuum decreased by a factor of 2 but then, over the next 15 s, increased again by a similar factor as more of the excavated ejecta move into the beam. The color temperature of the thermal emission from the dust is at least a factor of 2 cooler than in Fig. 11. Ejecta fill the slit at the start of the integration, having left the nucleus roughly a half second earlier. By the end of the integration, the slit is sampling material that could have left the nucleus as much as 1.3 s earlier traveling at lower velocity (these correspond to projected velocities on the order of 1 km/s). The succeeding spectrum shows that H_2O and CO_2 have decreased in intensity by a factor of 20 and also have become rotationally much cooler, whereas the level of the organic feature has decreased only by a factor of 6. The very strong organic feature (compared with Earth-based measurements of comets) suggests that we may be vaporizing organics that would not normally be vaporized in comets.

The observed temperature of the continuum (850 K) suggests that the center of the plume is even hotter and that the light we see in the MRI images is thermal emission. The peak brightness in the plume, i.e., the brightest part of the arch near the bottom of panels 9 and 10 in Fig. 7, can be used to constrain the nature of the ejecta. The initial decay in brightness is far too steep for simple expansion at constant velocity. Only after 0.42 s, i.e., beyond the end of the sequence in Fig. 10, does the brightness decay as t^{-2}, as would be expected for expansion at constant velocity of particles reflecting sunlight. The observed decline shown in Fig. 12 is consistent with blackbody radiation from a cloud of cooling particles. We modeled the plume as a 4000-kg cloud of liquid silicate droplets of 150 μm diameter, albedo 0.1, density 2.5 g cm^{-3}, expanding at 1.7 km/s, and with initial temperature 3500 K. The observed temperature of 850 K at the lateral boundary of the plume is consistent with this model (solid line in Fig. 12), because the temperature at the peak drops rapidly to 1000 K at the break in the solid curve near 0.3 s after the start of the plume. The model predicts that the hot plume would be optically thin after 0.03 s.

To measure compositional differences between the interior and the surface of the comet, we compare two spectra (Fig. 13) taken just off the limb of the nucleus, one 10 min before impact (ambient outgassing) and the other 4 min after it (excavated subsurface material). For both spectra, the slit was positioned roughly one nuclear radius, 3 km, from the southerly limb of the nucleus, with the slit oriented perpendicular to the radial direction and with width subtending 150 m and 57 m, respectively. The extracted spectra correspond to the median of 15 pixels along the slit on both sides of the antisaturation filter. These pixels correspond to positions roughly 1 km on both sides of the center of the slit for the preimpact spectrum and 400 m on both sides of the center of the slit for the postimpact spectrum. A continuum due to dust has been removed from the spectra in Fig. 13 to show the gaseous features. The dust spectrum consists of a slightly reddened solar-reflection spectrum, dominant at the shorter wavelengths, and postimpact thermal emission at 380 K, dominant at the longer wavelengths. Because this relatively late stage of excavation should be cool, the temperature excess above that of an isothermal black body at this distance (230 K) is likely due at least in part to the superheat required for particles that are small compared with the wavelength of peak thermal emission (*26*). The superheat would be larger than seen in other comets and suggests either the complete predominance of small particles compared with a component of large (cooler) particles in the ambient comae of other comets, or some residual heat from excavation, or a combination of the two.

The individual spectra of the gas (Fig. 13) had low signal-to-noise ratio compared with the

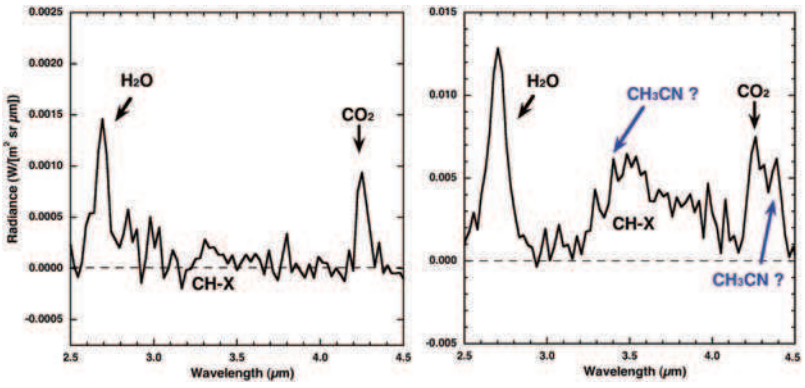

Fig. 13. Preimpact (–10 min, left) and postimpact (+4 min, right) spectra 3 km beyond the limb of the nucleus. The intensity scale differs by a factor of 6 between the two spectra. The abundance of organics relative to water increased substantially in the postimpact measurement.

signal of the nucleus, and the accuracy is limited primarily by the subtraction of the dark signal and the dust. The strong emission features are the same as those seen in the spectrum of the vapor plume, although relative abundances are different and the temperatures of the gases are much lower than those of the gases in Fig. 11. Even these emission features are optically thick in individual lines, so that absolute abundances cannot be obtained directly.

The most dramatic difference between the ambient outgassing and the excavated material was the large increase in organics. The abundances of HCN and CO_2 relative to H_2O also increased, but not as dramatically. Because the projected distance from the impact site to the field of view of the spectrometer was on the order of 4 km, material moving as slowly as 25 m/s (still well above escape speed) would have been excavated at 2 to 3 min into the excavation process and thus is material from far below the surface.

The feature at 4.40 μm is attributed to the ν_2 (CN stretch) band of methyl cyanide (CH_3CN). This species should also have its ν_1 (CH stretch) band at 3.38 μm, and this could correspond to the peak at that wavelength in the organic feature, a peak that is much weaker (and coincident with a methanol peak) in the preimpact spectrum. Other species with bands at 4.40 μm include HC_3N and HNCO. These are both ruled out by the absence of bands that should appear at other wavelengths. Nevertheless, we consider this identification very tentative because it appears to imply an excessively high abundance, although this may be due to optical depth effects. Ulich and Conklin (*27*) had identified methyl cyanide in a natural outburst of comet Kohoutek, but this result has been considered spurious. It is possible that the high abundance is incorrect as a result of errors in the assumed excitation of the molecule.

Summary and Conclusions

Comet Tempel 1 was thought to be a typical member of Jupiter's family of comets. The fact that the shapes and topographies of three comets in Jupiter's family (Borrelly, Wild 2, and Tempel 1) are so different from one another raises the question of whether any comet is typical when looked at closely. Both Borrelly and Tempel 1 have had long lifetimes in the inner solar system, whereas Wild 2 has not, but the differences between Borrelly and Tempel 1 are just as great as the differences between either of them and Wild 2. Tempel 1 is the first comet to show evidence for many classical impact craters. Tempel 1 also exhibits distinct layers with different topographic characteristics, a feature that may be common to all three of these comets. Tempel 1 exhibited frequent small outbursts, many of which were associated with an area near local sunrise. Because the nucleus also has little thermal inertia, this activity must be driven by material that is near the surface. We suspect that such activity may be common on other comets, but there are not sufficient data for any other comets to confirm this presumption. Although the surface temperatures, colors, albedos, and spectra indicate no ice on the surface, the rapid appearance of large amounts of volatiles in the earliest ejecta implies that ices are near the surface

The impact excavated a large volume of very fine (microscopic) particles, too many to have been pulverized in the impact itself; thus, they were preexisting either as very fine particles or as weak aggregates of such particles. This fine material must be tens of meters deep. From studying the ejecta at very late stages, the overall strength of the excavated material was determined to be <65 Pa, and the bulk density of the nucleus is estimated at roughly 0.6 g cm^{-3}. Initial ejecta were considerably hotter than 1000 K, but later stage ejecta were much cooler. The fastest material was moving at ~5 km/s, projected in the plane of the sky as seen from the spacecraft. The amount of organics relative to water increased considerably at the beginning of the outburst and, as the event progressed, the reduction in organics was much less than the reduction in H_2O and CO_2. The variation of CO_2 was similar but smaller. We have identified hydrogen cyanide (HCN) in the plume and suggest that methyl cyanide (acetonitrile, CH_3CN) could be present in the ejecta.

References and Notes

1. M. F. A'Hearn, M. J. S. Belton, A. Delamere, W. H. Blume, *Space Sci. Rev.* **117**, 1 (2005).
2. W. H. Blume, *Space Sci. Rev.* **117**, 23 (2005).
3. Information on instruments, data processing, and analysis is available on *Science* Online.
4. K. J. Meech *et al.*, *Science* **310**, 265 (2005).
5. M. J. S. Belton *et al.*, *Space Sci. Rev.* **117**, 137 (2005).
6. C. M. Lisse *et al.*, *Astrophys. J.* **625**, L139 (2005).
7. D. E. Brownlee *et al.*, *Science* **304**, 1764 (2004).
8. D. T. Britt *et al.*, *Icarus* **167**, 45 (2004).
9. C. Lisse, *Earth Moon Planets* **90**, 497 (2002).
10. A solar spectrum synthesized from various sources is available at the MODTRAN Web site (http://rredc.nrel.gov/solar/spectra/am0/modtran.html).
11. L. A. Lebofsky, J. R. Spencer, in *Asteroids II*, R. Binzel, Ed. (Univ. of Arizona Press, Tucson, AZ, 1989), pp. 128–147.
12. C. M. Lisse *et al.*, *Astrophys. J.* **625**, L139 (2005).
13. O. Groussin, P. Lamy, L. Jorda, *Astron. Astrophys.* **413**, 1163 (2004).
14. Y. R. Fernández, D. C. Jewitt, S. S. Sheppard, *Astron. J.* **123**, 1050 (2002).
15. J. R. Spencer, L. A. Lebofsky, M. V. Sykes, *Icarus* **78**, 337 (1989).
16. D. E. Brownlee *et al.*, *Science* **304**, 1764 (2004).
17. Z. Sekanina, D. E. Brownlee, T. E. Economou, A. J. Tuzzolino, S. F. Green, *Science* **304**, 1769 (2004).
18. P. H. Schultz, *J. Geophys. Res.* **101**, 21,117 (1996).
19. J. L. B. Anderson, P. H. Schultz, J. T. Heineck, *Meteorit. Planet. Sci.* **39**, 303 (2003).
20. P. H. Schultz, C. M. Ernst, J. B. Anderson, *Space Sci. Rev.* **117**, 207 (2005).
21. J. E. Richardson, H. J. Melosh, A. Artemeiva, E. Pierazzo, *Space Sci. Rev.* **117**, 241 (2005).
22. K. R. Housen, K. A. Holsapple, M. E. Voss, *Nature* **402**, 155 (1999).
23. H. J. Melosh, *Impact Cratering: A Geologic Process* (Oxford Univ. Press, New York, 1989).
24. R. M. Schmidt, K. R. Housen, *Int. J. Impact Eng.* **5**, 543 (1987).
25. K. R. Housen, R. M. Schmidt, K. A. Holsapple, *J. Geophys. Res.* **88**, 2485 (1983).
26. L. Kolokolova, M. S. Hanner, A.-Ch. Levasseur-Regourd, B. Å. S. Gustafson, in *Comets II*, M. C. Festou, H. U. Keller, H. A. Weaver, Eds. (Univ. of Arizona Press, Tucson, AZ, 2004), pp. 577–604.
27. B. L. Ulich, E. K. Conklin, *Nature* **248**, 121 (1974).
28. The outburst of June 14 was first reported on the DI Collaborators' Network by L.-M. Lara, based on observations at Calar Alto. It was then found easily in the data from the spacecraft. The later ones were found in near-real time in the spacecraft data. The outburst of June 22 was observed simultaneously and serendipitously with the Hubble Space Telescope. The earlier outbursts were found during the rotational analysis.
29. This work was funded by NASA through its Discovery Program, with a contract to the University of Maryland and a task order to the Jet Propulsion Laboratory. In addition to the referees, M. Mumma and D. Bockelée-Morvan provided helpful comments.

Supporting Online Material

www.sciencemag.org/cgi/content/full/1118923/DC1
Materials and Methods
Fig. S1
Table S1
References

16 August 2005; accepted 1 September 2005
Published online 8 September 2005;
10.1126/science.1118923
Include this information when citing this paper.